4-1-2021

Measurements and Analysis of Propagation Channels in Vehicle-to-Infrastructure Scenarios

Wei Li

Xiaoya Hu

Jie Gao

Lian Zhao

Xuemin Shen

IEEE Transactions on Vehicular Technology, Vol. 69, No. 4 (April 2020): 3550-3561. DOI.

Measurements and Analysis of Propagation Channels in Vehicle-to-Infrastructure Scenarios

Wei Li
Wuhan National Laboratory for Optoelectronics, School of Electronics Information and Communications, Huazhong University of Science and Technology, Wuhan, China
Xiaoya Hu
Key Laboratory of Image Processing and Intelligence Control, School of Artificial Intelligence and Automation, Huazhong University of Science and Technology, Wuhan, China
Jie Gao
Department of Electrical and Computer Engineering, University of Waterloo, Waterloo, Canada
Lian Zhao
Department of Electrical, Computer and Biomedical Engineering, Ryerson University, Toronto, Canada
Tao Jiang

Wuhan National Laboratory for Optoelectronics, School of Electronics Information and Communications, Huazhong University of Science and Technology, Wuhan, China

Abstract:

In this paper, we present measurements and analysis of propagation channels in vehicle-to-infrastructure (V2I) scenarios, which are the basis of designing vehicular communication systems. Firstly, we propose a deterministic geometry-based method to classify V2I links into three types, i.e., line-of-sight beneath (LOS-B), non-LOS (NLOS), and line-of-sight above (LOS-A), based on the environmental features, where roadside row of trees constitute the main obstacles. Secondly, for each link, we investigate the large-scale fading effect on V2I channels, including the path loss exponent and shadowing components. Subsequently, we validate the empirical path loss model using extensive measurements and two classical channel models. The results show a good fit with a near-zero mean and tolerable standard deviation of the estimation error. Finally, we analyze the small-scale fading effects, including fading depth and distance-dependent Ricean K-Factor, which are very important for accurately predicting the required fading margin and link budget. Through the analysis and simulations, this work provides a reference of the V2I channel characteristics for the test, design, and performance analysis of V2I communication systems.

SECTION I. Introduction

Vehicular ad-hoc networks (VANETs) has been an attractive research area since VANETs are expected to support various applications for intelligent transportation system (ITS), such as traffic congestion control, accident avoidance, and multimedia services [1], [2]. Existing works have validated the use of IEEE 802.15.4-compliant devices to achieve reliable vehicular communications [3]–[4][5][6]. For many VANETs-related applications, especially safety related ones, it is crucial to precisely model the vehicular channel attenuation. In general, vehicular channels mainly consist of vehicle-to-vehicle (V2V) and vehicle-to-infrastructure (V2I) channels. The V2V channels have been intensively studied [7]–[8][9][10], and both deterministic and statistical models have been proposed. In contrast, V2I channel models are not nearly as researched as those of V2V channels. This research gap may be due to the resemblance between V2I channels and cellular communication channels: one of the communicating pairs (base station) is stationary, while the other (user equipment) is mobile. However, the propagation characteristics of V2I communications are very different from those of cellular channels, especially regarding the carrier frequency, communication range, and antenna height [11]. Therefore, establishing V2I channel models is essential to fill the mentioned research gap and support V2I communication coverage prediction and interference analysis in VANETs system.

Vehicular channel models can be divided into three categories: geometry-based deterministic (GBD) models, geometry-based stochastic (GBS) models, and non-geometrical stochastic (NGS) models [12]. The ray-tracing method falls under the scope of GBD models, which needs detailed environmental database and high computational capability to accurately model all possible propagation paths from the Tx to the Rx, including LOS, reflection, diffraction, and scattering components. GBS models also take into account the geometrical properties of the surrounding objects, but they calculate the channel statistics either from measurements or simulations. NGS models generate channel statistics in a completely stochastic fashion, where both the geometrical properties and the channel statistics are generated stochastically [11]. In general, GBS models are more computationally efficient than GBD models and can obtain higher prediction accuracy than NGS models. Therefore, we apply GBS models considering the trade-off between complexity and precision in the design of V2I communication systems.

Existing empirical path loss models mainly focus on either V2V or cellular channels, and are not applicable to V2I channels. In this paper, we aim to apply a geometry-based stochastic path loss model to fill this gap. Furthermore, we present a microscopic analysis of shadowing and small-scale fading effects in V2I channels. Since the link-level classification is necessary to obtain the complete statistic characterization and channel property in vehicular communications [8], we firstly classify V2I communications into three link types based on the relative height between the elevated infrastructure (i.e., the antennas deployed on lamps) and the row of trees. Based on the different link types, we investigate the relation between path loss exponent and the infrastructural height. The shadowing component is fitted with log-normal distribution, and small-scale fading effects, including fading depth and distance-dependent Ricean K-factor, are also studied. These channel characterizations can be used for VANETs simulators and performance analysis, e.g., capacity calculation and coverage prediction [13].

The major contributions of this paper are as follows:

1. Considering the features of a typical V2I scenario where the main obstructions are roadside row of trees, we propose a novel three-segment link classification method based on rigorous geometrical analysis.
2. We analyze the large-scale fading of V2I channels, including the path loss and shadow fading. The extensive measurements verify the empirical path loss model.
3. The small-scale fading analysis is presented to get a full picture of the channel characteristics. It can be used for performance evaluation and optimization of different transmission schemes over V2I channels.

The remaining part of this paper is structured as follows: We review related works in Section II and introduce the measurement setup in Section III. Section IV describes a geometry-based classification method to distinguish three different link types. We analyze the respective path loss exponent and shadow fading of the different link types, and validate the empirical path loss model with extensive measurements in Section V. The small-scale fading analysis is presented in Section VI. Finally, Section VII elaborates the conclusion of this work.

SECTION II. Related Works

Extensive studies have been conducted on vehicular channel models in different VANETs environments. Maurer *et al.* [14] modeled roadside structures, such as buildings, parked vehicles, and trees, as scattering objects, and used the ray-tracing method to capture the variation of inter-vehicular path loss in a simulated scenario. Boban *et al.* [8] proposed an efficient geometry-based channel model for V2V communications on specific link types (i.e., LOS, NLOS by vehicles, and NLOS by buildings/foliage) in different scenarios, such as urban, suburban, and highway environments. Their proposed model, GEMV2, greatly reduced the computational complexity while guaranteeing the link-level prediction accuracy. Acosta-Marum *et al.* [15] conducted vehicular communication measurements in six different environments, three for V2V channels and three for V2I channels, in urban, suburban, and highway scenarios. However, the authors only analyzed small-scale fading without estimating the path loss or lognormal shadowing. Chelli *et al.* [16] proposed a novel V2I channel model of small scale fading for a blind corner scattering environment, which provides a better characterization of V2I propagation variations but does not cover the path loss model either.

He *et al.* [17] proposed an empirical path loss model for high-speed railway viaduct scenarios, which investigated the influence of viaduct height and base station relative height on the path loss exponent and analyzed the fading behavior. However, the proposed model can be applied to railway communications but not vehicular communications because their carrier frequency, antenna height, and surrounding scatters are significantly different. The coverage and capacity requirements of digital broadcasting, cellular, and dedicated short-range communication (DSRC) to implement the V2I communication system were studied in [13]. Particularly, for the

DSRC-V2I systems, Belanovic *et al.* investigated the potential path loss model with coverage less than 1 km and antenna height varying from 1 m to 10 m and concluded that the path loss estimate has upper and lower bounds determined by the COST-Hata model and the inter-vehicle model, respectively.

Gozalvez *et al.* [18] conducted extensive field testing on the link quality of IEEE 802.11p V2I channels in urban scenarios. They qualitatively analyzed the influence of trees at various infrastructural antenna heights and emphasized the importance of separating the BS antenna from nearby obstacles to improve the propagation conditions. Meng *et al.* [19] proposed an empirical near-ground path loss model while considering the frequency, antenna height, and foliage depth in forested environment at VHF and UHF bands. The integrated model combined both the foliage-induced attenuation and ground-reflected component. The predicted path loss fitted well with measurements. Nevertheless, this empirical model derived from static foliage attenuation measurements is not suitable for V2I communications. Aygun *et al.* [20] proposed a geometry-based propagation model for NLOS link obstructed by foliage in an urban V2I scenario and validated it with realistic data [18]. However, they did not concretely analyze the effect of infrastructural antenna height on path loss, and the calculation of penetration depth in foliage was not provided. Li *et al.* [21] proposed a geometry-based deterministic path loss model considering the foliage-induced attenuation for V2I communications. Although this model can accurately predict the received signal strength with the variability of Tx-Rx separations at different infrastructural antenna heights, it is too computationally expensive to be used for large-scale simulations in VANETs. In this paper, we investigate both the large-scale and small-scale fading effects to attain a comprehensive knowledge of the V2I channels. We start by introducing the measurement setup in the following section.

SECTION III. Measurement Setup

We conducted a series of experiments to analyze the channel characteristics using IEEE 802.15.4-compliant devices in a typical V2I scenario, where obstacles like buildings and vehicles were scarce and planted trees were the major obstacles blocking the LOS link, as shown in Fig. 1. We assume that roadside trees (approximately the same species and size) are planted in rows and evenly distributed in a single V2I cell radius. This scenario is common on some urban, suburban, and rural roads where the environment needs to stay homogeneous and harmonious. Completely irregular situations are not within the scope of this paper.

Fig. 1. Experimental scenario. (a) The transmitting antenna was placed on the roof of the test vehicle to minimize the multipath effect produced by the car. (b) The receiving antenna was placed on the road lamp post. Its height varies from 1 m to 9 m with an interval of 1 m.

The experimental system was composed of two nodes with TI CC2530 chip and IEEE 802.15.4 Zigbee protocol stack, one as a moving transmitter (Tx) and the other as a fixed receiver (Rx). The Tx was placed on the vehicle roof (approximately 1.6 m above the ground) moving at a fixed speed of 50 km/h. The Rx was placed on a road lamp post, and its height varies from 1 m to 9 m with an interval of 1 m. The parameters of the two nodes were

configured as follows: the signal carrier frequency, bandwidth, and maximum transmission power were set to 2.4 GHz, 2 MHz, and 4.5 dBm, respectively. We chose the dipole antenna, which is omnidirectional and linearly polarized for both the Tx and Rx. The antenna gain was set to 3.5 dBi. The measured received signal power was averaged at interval of 40 times wavelength (approximately 5 m) to analyze the large-scale fading variations. In addition, we selected a 10 cm sampling interval from measurements to investigate the small-scale fading effect.

SECTION IV. Classification of Link Types

Accurately classifying the links of vehicular communications is particularly important for safety applications, and the goal is to determine whether the vehicle will receive a safety-critical message or not [8], [22]–[23][24]. Therefore, according to the geometrical features of the vehicular scenario, we classify V2I communications into different link types to establish a proper empirical path loss model. The link types are classified into three different cases, as shown in Fig. 2(a):

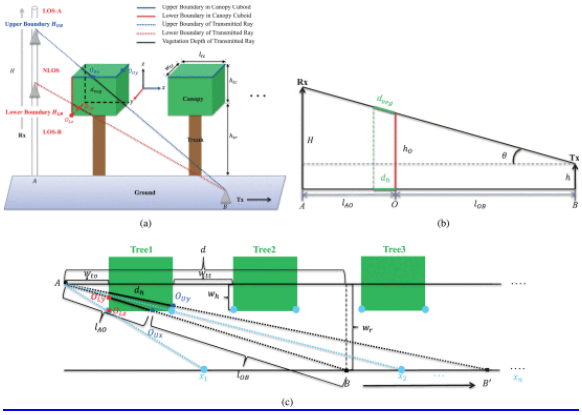

Fig. 2. A 3-D diagram for boundaries calculation and its sectional view and top view. (a) A 3-D diagram for characterizing the generation process of boundaries. (b) Sectional view of the diagram including line *AOB*. (c) Top view of the diagram and some notations for geometrical calculation.

- **LOS-B**—links that involve the LOS ray being transmitted beneath the tree canopy;
- **NLOS**—links that involve the LOS ray being obstructed by the tree canopy;
- **LOS-A**—links that involve the LOS ray being transmitted above the tree canopy.

In the vehicular scenario, roadside trees are considered as the main obstacles. A leafy tree consists of a canopy and a trunk. The canopy can be modeled as a cuboid [25], as shown in Fig. 2(a). When the vehicle travels on the road, for any given position of the vehicle, there are two thresholds of antenna height, H_{LB} and H_{UB}, that relates to the obstruction of the LOS link. The two thresholds determine the range of height in which the LOS link is obstructed by the tree canopy at a given distance. The calculation of H_{LB} and H_{UB} is given as follows.

A. Analysis of the Lower Boundary H_{LB}

In order to describe their geometrical relations, we provide some illustrations in Fig. 2 and add some corresponding notations (see Table I). Using geometry theory, it is not hard to find that the lower boundary ray is limited by the two red edges of the first tree's canopy cuboid in Fig. 2(a). The latter trees affect the upper boundary, not the lower boundary. Therefore, we discuss them in two cases: the lower boundary ray intersects the y-axis red line and the z-axis red line of the first tree, respectively.

TABLE I Notations

Symbol	Explantation	Value
H	Height of the Rx	[1,9]
h	Height of the Tx	1.6
d	Horizontal distance between Tx and Rx	[30,300]
w_{to}	Width between Tree1 and the Rx	2.45
w_{tt}	Width between two neighbouring trees	3.4
w_r	Width of the Tx and the Rx	5.7
w_h	Half of the tree canopy's width	0.75
l_{tc}	Length of the tree canopy	2.1
w_{tc}	Width of the tree canopy	1.5
h_{tc}	Height of the tree canopy	2
h_{tr}	Height of the tree trunk	4.2
O_U	Intersection of upper boundary ray and canopy	NaN
O_L	Intersection of lower boundary ray and canopy	NaN
d_{veg}	Vegetation depth through the tree canopies	NaN
d_h	Horizontal projection of vegetation depth	NaN

Case 1: The lower boundary ray and the y-axis red line intersect at point OLy.

From Fig. 2(b) and Fig. 2(c), we obtain the following formulas:

$$\frac{w_{to}}{d} = \frac{l_{AO_{Ly}}}{l_{AO_{Ly}} + l_{O_{Ly}B}}$$

$$\frac{h_o - h}{H_{LB-y} - h} = \frac{l_{OB_{Ly}}}{l_{AO_{Ly}} + l_{O_{Ly}B}}$$

(1)(2)

Then we obtain:

$$H_{LB-y} = \frac{d \cdot (h_o - h)}{d - w_{to}} + h$$

(3)

The relation between H_{LB-y} and d is plotted by the red solid line in Fig. 3. Note that H_{LB-y} reaches its minimum $min(H_{LB})$ at the cell radius (i.e., 300 m in our scenario), and the minimum value is 4.2214 m.

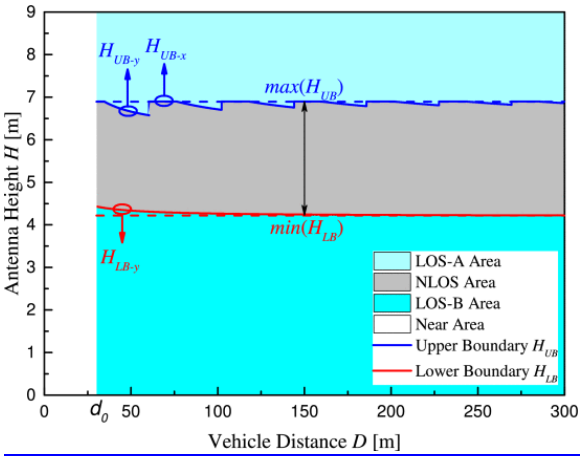

Fig. 3. Link types of different areas. We can easily classify any given coordinate (D, H) into its corresponding area from this figure. When $H < min(H_{LB})$, the LOS ray is transmitted beneath the tree canopy and is abbreviated as LOS-B. If $min(H_{LB}) < H < max(H_{UB})$, the ray is transmitted through a NLOS link due to the obstruction of tree canopy. Otherwise, the LOS ray passes above the tree canopy, named LOS-A.

Case 2: The lower boundary ray and the z-axis red line intersect at point O_{Lz}.

Similarly, we obtain the following formula from Fig. 2(c):

$$\frac{w_{to}}{d} = \frac{w_h}{w_r}$$

(4)

Then, we obtain $d = 18.62$ m from the measurements in our scenario. Substituting this value into Formula (3), we obtain $H_{LB-z} = 4.594$ m. This means that when the vehicle moves further than 18.62 m, the infrastructural antenna height should be under 4.594 m. Otherwise, the LOS ray will enter the canopy cuboid. However, we only consider Tx-Rx distance larger than 30 m to filter out the near-field effect, which is mainly affected by the antenna height and radiation pattern. Thus, Case 2 is neglected and the variable H_{LB-y} is used to characterize H_{LB}.

B. Analysis of the Upper Boundary H_{UB}

Similarly, the upper boundary H_{UB} is determined by the two blue edges of the neighboring tree's canopy cuboid in Fig. 2(a).[1] We also discuss them in two cases: the higher boundary ray intersects the x-axis blue line and the y-axis blue line.

Case 1: The upper boundary ray and the x-axis blue line intersect at point O_{Ux}.

From Fig. 2(c), we can obtain:

$$\frac{w_h}{w_r} = \frac{l_{AO_{Ux}}}{l_{AO_{Ux}} + l_{O_{Ux}B}}$$

(5)

From Fig. 2(b), we can obtain:

$$\frac{h_o - h}{H_{UB-x} - h} = \frac{l_{O_{Ux}B}}{l_{AO_{Ux}} + l_{O_{Ux}B}}$$

(6)

Combine Formula (5) with (6):

$$H_{UB-x} = \frac{w_r \cdot (h_o - h)}{w_r - w_h} + h$$

(7)

This result tells us that the intersection point O_{Ux} remains at a fixed height H_{UB-x}, which is irrelevant to distance d. When we set $h_o = h_{tr} + h_{tc}$, we can obtain the fixed maximum $H_{UB-x} = 6.897$ m in our scenario, denoted by the blue solid horizontal line in Fig. 3.

Case 2: The upper boundary ray and the y-axis blue line intersect at the point O_{Uy}.

In this case, we introduce some fixed points x_n, which represent the intersections between vehicle route and the lines that connect point A and the vertices of rectangle in Fig. 2(c). Then, we obtain the following equation:

$$x_n = \begin{cases} \frac{w_r}{w_h} \cdot \left[w_{to} + (l_{tc} + w_{tt}) \cdot \frac{n-1}{2}\right] & \text{if } n \text{ is odd,} \\ \frac{w_r}{w_h} \cdot \left[w_{to} + l_{tc} \cdot \frac{n}{2} + w_{tt} \cdot \frac{n-2}{2}\right] & \text{if } n \text{ is even.} \end{cases} (n = 1,2 \dots) \quad (8)$$

We define a new symbol $d_{AO_{Uy}}$, meaning the horizontal distance between point A and point O_{Uy}. Let $d \in (x_n, x_{n+1}), n = 1,2 \dots$

$$d_{AO_{Uy}} = \begin{cases} 0 & \text{if } n \text{ is odd,} \\ w_{to} + l_{tc} \cdot \frac{n}{2} + w_{tt} \cdot \frac{n-2}{2} & \text{if } n \text{ is even.} \end{cases}$$

(9)

From Fig. 2(c), we can obtain:

$$\frac{d_{AO_{Uy}}}{d} = \frac{l_{AO_{Uy}}}{l_{AO_{Uy}} + l_{O_{Uy}B}}$$

(10)

Similarly, in the Fig. 2(c),

$$\frac{h_o - h}{H_{UB-y} - h} = \frac{l_{O_{Uy}B}}{l_{AO_{Uy}} + l_{O_{Uy}B}}$$

(11)

Substitute Formula (10) into Formula (11), we can obtain:

$$H_{UB-y} = \frac{d \cdot (h_o - h)}{d - d_{AO_{Uy}}} + h$$

(12)

From Fig. 3, we observe that the blue solid line presents two different trends, i.e., one remains constant (see segment H_{UB-x}) and the other decreases with distance (see segment H_{UB-y}). For the two trends, there exists a common maximum value, $max(H_{UB}) = 6.897$ m, in our scenario. Meanwhile, the variation of the red solid line is subject to H_{LB-y} and reaches a minimum value (denoted by $min(H_{LB})$) of 4.221 m. In conclusion, the spatial variation of the lower boundary H_{LB} and the upper boundary H_{UB} can be obtained based on the above analysis. Given a coordinate (vehicle distance, infrastructure height), named (D, H), we can classify it into one of the three different areas shown in Fig. 3. Specifically, the values $min(H_{LB})$ and $max(H_{UB})$ are mainly determined by $min(H_{LB-y})$ and $max(H_{UB-x})$, as shown in Formula (3) and (7). It means that we can use four parameters to achieve a precise classification of different link types. In the following section, we analyze the large-scale fading effect based on this classification method.

SECTION V. Large-Scale Fading Analysis for V2I Channel

In this paper, we adopt a widely-used empirical model to characterize the spatial variation of received signal strength (RSS), i.e., the path loss and fading model [26], shown as follows:

$$PL(d) = PL(d_0) + 10n\log_{10}\left(\frac{d}{d_0}\right) + X_\sigma + Y$$

(13)

where $PL(d_0)$ is the intercept decibel path loss at the reference distance d_0; n is the path loss exponent; d is the distance that the vehicle has moved; and X_σ and Y are the shadowing and small-scale fading contributions respectively. The shadow fading component X_σ is a zero-mean Gaussian distributed random variable with standard deviation σ, describing the random shadowing, whereas Y is modeled as a Rician, Rayleigh, Nakagami, or Weibull distributed variate [26]. We set d_0 to 30 m based on our measurements [21].

In this section, we aim to investigate the large-scale fading components, including the path loss exponent n and the shadow fading component X_σ. The small-scale fading component Y will be introduced in the next section. In the following analysis, we fix the intercept at $PL(d_0) = 20\log_{10}(4\pi(d_0/\lambda)) = 69.82$ dB. Then, we estimate the path loss exponent n under various heights and analyze the shadowing component X_σ through the least-square regression method. Both the path loss and shadow fading components are estimated according to the different link types in Section IV. The detailed parameters to be estimated are listed in Table II.

TABLE II Large-Scale Fading Parameters for Different Link Types

Antenna Height	Link Type	Large-scale Parameters
$H \leq \min(H_{LB})$	LOS-B	$n_{LOS-B}, X_{\sigma LB}$
$\min(H_{LB}) < H \leq \max(H_{UB})$	NLOS	$n_{NLOS}, X_{\sigma NL}$
$H > \max(H_{UB})$	LOS-A	$n_{LOS-A}, X_{\sigma LA}$

For the different link types (LOS-B, NLOS, LOS-A), we plot the points of path loss exponent n from four tests under different infrastructural antenna heights, as shown in Fig. 4. Then we apply several of the three fitting

models (linear model and quadratic model and hyperbola model)[2] to explain the relationship between the path loss exponent n and the antenna height H in different links, as follows:

$$\text{Linear Model: } n = c_1 H + z$$
$$\text{Quadratic Model: } n = c_1 H^2 + c_2 H + z$$
$$\text{Hyperbola Model: } n = c_1 H + c_2 / H + z$$

(14)(15)(16)

where $c_i (i = 1,2)$ and z are unknown variables.

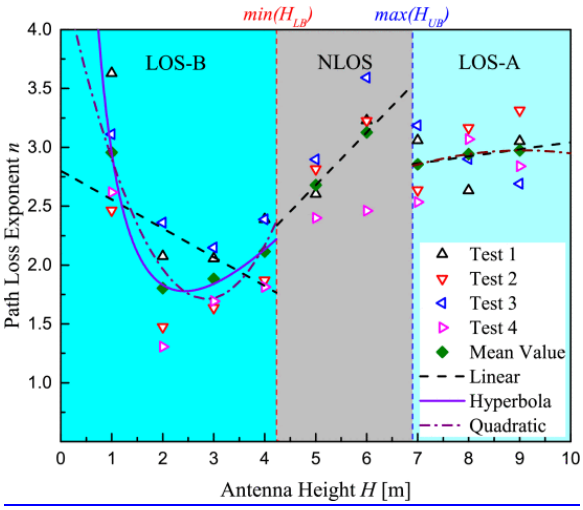

Fig. 4. The discrete points with triangular marks denote the values of path loss exponent, n, in four tests, and the diamond marks denote the mean value at respective infrastructural antenna height, H. The plotted lines represent the fitting results of the three different fitting models to approach the mean values. The filled areas with different colors represent three different links, which are separated by two vertical dashed lines, $H = min(H_{LB})$ and $H = max(H_{UB})$ respectively, as shown in Fig. 3.

The fitting curves of these three models are shown in Fig. 4, and the detailed fitting analysis is presented in the following sections. Several metrics are applied to measure the fitting precision, i.e., the $Sum\ of\ Squared\ Residuals\ (SSR)$, $Root\ Mean\ Square\ Error\ (RMSE)$, and $R-square$. SSR and $RMSE$ can be used to measure the discrepancy between the measured data and the estimation. For SSR and $RMSE$, if the value is closer to 0, the predicted result will be more exact. On the contrary, $R-square$ indicates better estimation accuracy when its value is closer to 1. The calculated results are given in Table III. In a subsequent study, we will investigate the propagation characteristics and fitting performance of these three link types, LOS-B, NLOS, and LOS-A.

TABLE III Model Parameters for Different Link Types

Parameters	LOS-B Area			NLOS Area	LOS-A	Area
	Linear	Hyperbola	Quadratic	Linear	Linear	Quadratic
c_1	-0.2446	0.5743	0.34606	0.44808	0.05993	-0.02849
c_2	None	3.389	-1.97496	None	None	0.51577
z	2.801	-1.012	4.53105	0.43814	2.44414	0.63977
SSR	0.5372	0.00287	0.05817	0	5.4112E-4	0
$RMSE$	0.5183	0.05358	0.24119	NaN	0.02326	NaN

$R-square$	0.3578	0.9966	4.53105	1	0.92995	1

A. Large-Scale Fading Analysis for LOS-B Link

The points plotted in the LOS-B in Fig. 4 show that the mean value of path loss exponent reaches its minimum at $H = 2$ m and increases with the antenna height. In particular, the value at $H = 1$ m reaches its maximum in LOS-B area since the Rx is located near the ground, and the received signal is severely affected by the abundant obstacles surrounding the Rx. The results confirm that if the roadside node is placed at the same height as vehicles, approximately 2 m, the best communication performance may be achieved.

From the comparative results of the three fitting models in Table III, we observe that the hyperbola model is better than the linear and quadratic model, with larger $R-square$ and smaller SSR and $RMSE$. Therefore, we choose the hyperbola model as the final model to describe the influence of H on n in the LOS-B link. Then, the path loss exponent n of the LOS-B link can be written as follows:

$$n_{LOS-B} = 0.574H + 3.389/H - 1.012, H \leq min(H_{LB})$$

(17)

Subsequently, the shadow fading component $X_{\sigma LB}$ is fitted with a normal distribution function and the fitting curve is plotted in Fig. 5(a). The parameters of $X_{\sigma LB}$ are calculated by least-squares regression methods, the mean value μ is 0.533, and the standard deviation σ is 0.497.

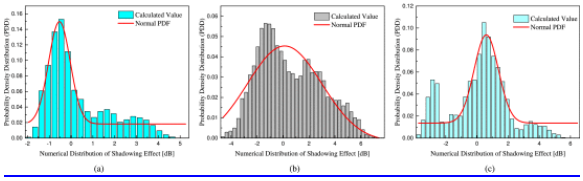

Fig. 5. The shadowing analysis for different link types. All of them follow a distribution with near-zero mean and acceptable standard deviation. The numerical distribution of shadowing effect is more dispersed in NLOS area. (a) Probability distribution function (PDF) of shadowing effect $X_{\sigma LB}$ for LOS-B link. It is fitted to normal distribution $X_{\sigma LB}$~N(0.533,0.497). (b) PDF of shadowing effect $X_{\sigma NL}$ for NLOS link. It is fitted to normal distribution $X_{\sigma NL}$~N(0.124,2.865). (c) PDF of shadowing effect $X_{\sigma LA}$ for LOS-A link. It is fitted to normal distribution $X_{\sigma LA}$~N(0.6,0.78).

B. Large-Scale Fading Analysis for NLOS Link

Limited by the small size of the tree canopy cuboid and relatively large experimental interval of antenna height in our measurements, only two sets of NLOS data can be used to analyze the relationship between antenna height and path loss exponent, i.e., $H = 5$ m and $H = 6$ m. Therefore, we apply the linear model to characterize the trend of the path loss exponent. The detailed calculation results and fitting curve are shown in Table III and Fig. 4, respectively. The final fitting function is as follows:

$$n_{NLOS} = 0.448H + 0.438, min(H_{LB}) < H \leq max(H_{UB})$$

(18)

However, this model may be over-fitted, and minute height interval experiments should be conducted to analyze the precise influence generated by the canopy cuboid in the future. In Fig. 4, the path loss exponent n reaches its maximum at $H = 6$ m, which means that the transmitted signal endures the severest channel attenuation. When considering their physical size, we find that the vegetation depth of tree canopies

reaches a maximum at $H = 6$ m, where the received power decreases extremely. We calculate the theoretical values of vegetation depth at different heights in NLOS area, which have positive correlation with the path loss exponent. This aspect of content is discussed in the following. The shadow fading component $X_{\sigma NL}$ of the NLOS link is fitted and plotted in Fig. 5(b). The mean value and standard deviation of $X_{\sigma NL}$ are 0.124 and 2.865, respectively.

The relationship between vegetation depth and antenna height: The vegetation depth d_{veg} (shown as the black solid line in Fig. 2(a)), has a direct influence on channel attenuation [19], [20], [25]. Therefore, it relates to the path loss exponent n. However, with the scarce measurement data in the NLOS area, we have to investigate the relation between d_{veg} and H instead of that between n and H.

From Fig. 2(b) and Fig. 2(c), we obtain the following formulas: when $d \in (x_n, x_{n+1})$, and $n = 1,2 \ldots$,

$$d_h = \frac{\sqrt{{w_r}^2 + d^2}}{d} \cdot \begin{cases} \left(\frac{d \cdot w_h}{w_r} - w_{to} - \frac{n-1}{2} \cdot w_{tt}\right) & \text{if } n \text{ is odd,} \\ \frac{n}{2} \cdot l_{tc} & \text{if } n \text{ is even.} \end{cases}$$

$$d_{veg} = \frac{d_h}{\cos\theta}$$

$$\tan\theta = \frac{H - h}{l_{AO} + l_{OB}}$$

$$l_{AO} + l_{OB} = \sqrt{{w_r}^2 + d^2}$$

(19)(20)(21)(22)

$$\text{When } d \in (x_n, x_{n+1}), n = 1,2 \ldots, d_{veg} = \frac{\sqrt{{w_r}^2 + d^2 + (H-h)^2}}{d} \cdot \begin{cases} \left(\frac{d \cdot w_h}{w_r} - w_{to} - \frac{n-1}{2} \cdot w_{tt}\right) & \text{if } n \text{ is odd,} \\ \frac{n}{2} \cdot l_{tc} & \text{if } n \text{ is even} \end{cases}$$

(23)

Then we obtain Formula (23), shown at the bottom of this page. From it, we find that the variable d_{veg} depends on the variables H and d. The relationship between them is plotted in Fig. 7(a), in which the vegetation depth d_{veg} is mainly affected by the vehicle distance d, whereas the influence of the antenna height H is relatively vague. In order to analyze the effect of the antenna height H on the vegetation depth d_{veg}, we highlight this part in Fig. 7(b) and find that every 0.5 m elevation in H will only cause an increase of 0.001 m in d_{veg}. However, the phenomenon of slow linear increase in d_{veg} due to increase in H reflects the same variation tendency between n and H (shown in the NLOS area in Fig. 4) to some extent. A more precise relationship between them could be explored in the future.

C. Large-Scale Fading Analysis for LOS-A Link

When the infrastructural antenna height continues to increase, the transmitted signal enters into the LOS-A area. From Fig. 4, we observe that the path loss exponent, n, in LOS-A area is larger than that in LOS-B area. The reason for this phenomenon may be as follows: although the LOS link exists, the other main ray reflected by the ground may still be obstructed by the tree canopy cuboid, which generates a non-negligible path loss. The other possible reason may be the radiation pattern of antenna. However, this effect caused by different infrastructural heights has been analyzed in our previous work [21, Sec. III-B], and the conclusion verified that the antenna gain remains at the maximum value in the far zone and is not related to the infrastructural height. Based on the comparison of results in Table III, we choose quadratic as the final model for LOS-A area, which is written as follows:

$$n_{LOS-A} = -0.028H^2 + 0.516H + 0.64, H > max(H_{UB})$$

(24)

Also, the shadow fading component, $X_{\sigma LA}$, is fitted and plotted in Fig. 5(c). The mean value and standard deviation of $X_{\sigma LA}$ are $\mu = 0.6$ and $\sigma = 0.78$.

D. Empirical Path Loss Modelling for V2I Scenario

On the basis of the above, the overall path loss model can be written as Formula (25), shown at the bottom of this page, in which the path loss exponents n_{LOS-B}, n_{NLOS}, and n_{LOS-A} are calculated and represented as Formula (17), (18), and (24), respectively. The shadowing effect component follows the near-Gaussian distribution, in which $X_{\sigma LB} \sim N(0.533,0.497)$, $X_{\sigma NL} \sim N(0.124,2.865)$, and $X_{\sigma LA} \sim N(0.6,0.78)$.

$$PL(d) = PL(d_0) + \begin{cases} 10n_{LOS-B}\log\left(\frac{d}{d_0}\right) + X_{\sigma LB} & H \le \min(H_{LB}) \\ 10n_{NLOS}\log\left(\frac{d}{d_0}\right) + X_{\sigma NL} & \min(H_{LB}) < H \le \max(H_{UB}) \\ 10n_{LOS-A}\log\left(\frac{d}{d_0}\right) + X_{\sigma LA} & H > \max(H_{UB}) \end{cases}$$

(25)

E. Empirical Path Loss Model Validation

Owing to the very limited existing research on V2I channel models [11], we have no other empirical models to perform comparisons. Therefore, we only evaluate the fitted empirical model[3] by comparing it with the measured RSS and the other two classical path loss models, i.e., free-space model [27, Sec. 2.3] and two-ray model [27, Sec. 2.4.1]. The empirical model is calculated as follows:

$$\begin{aligned} P_r &= P_t + 2G_{ag} - PL(d) \\ &= \underbrace{P_t + 2G_{ag} - PL(d_0)}_{\text{Intercept}} - 10n\log_{10}\left(\frac{d}{d_0}\right) - X_\sigma \end{aligned}$$

(26)

where P_r is the RSS; P_t is the transmitted power; G_{ag} is the gain of antenna;[4] $PL(d)$ is the decibel path loss and the intercept is a constant value of -58.32.

The free-space model can be calculated as follows,

$$P_r = P_t + 2G_{ag} - 20\log_{10}\left(\frac{4\pi l}{\lambda}\right)$$

(27)

where λ is the wave length, and l is the real distance between Tx and Rx.

The two-ray model is presented as follows,

$$P_r = P_t - 20\log_{10}\left|\frac{4\pi}{\lambda}\right| + 20\log_{10}\left|\frac{\sqrt{G_l}}{l} + \frac{R_\perp\sqrt{G_r}e^{-j\triangle\varphi}}{d_1 + d_2}\right|$$

(28)

where $d_1 + d_2$ is the total distance of the reflected ray; $\sqrt{G_l}$ and $\sqrt{G_r}$ are the products of the transmitting and receiving antenna field radiation patterns in the LOS and reflected ray respectively [27]; $\triangle\varphi$ is the phase difference between two rays; and $R_\perp$ is the ground reflection coefficient.

We plot the fitting results in three different areas in Fig. 6 and the statistics results of the error analysis in Fig. 8, in which the columns represent the mean error and the lines represent the standard deviation. It is not hard to find that the proposed model has the best fitting performance with a near-zero mean compared with the other two models. We analyze the channel properties and estimation accuracy of the three areas.

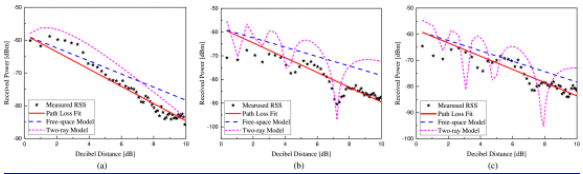

Fig. 6. Model validation with measurements and two classical path loss models in three areas. (a) Model validation in LOS-B area. (b) Model validation in NLOS area. (c) Model validation in LOS-A area.

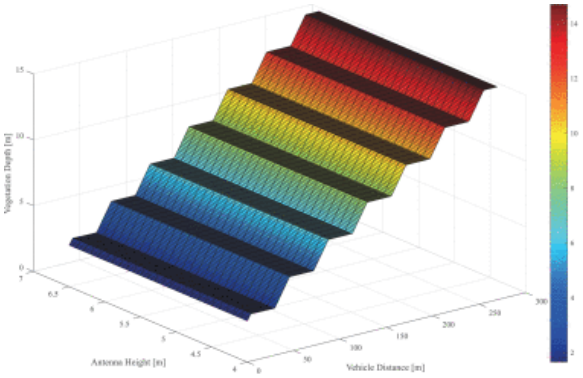

(a)

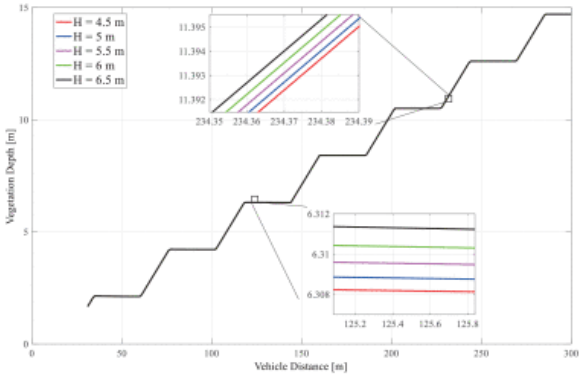

(b)

Fig. 7. Obviously, d_{veg} increases with d in a staged way due to the property of piecewise function in Formula (23). Probably limited by the small size of canopy cuboid, d_{veg} increases very slowly with H. We have to magnify the lines into the scale of 0.001 m to observe their variation tendency in Fig. 7(b), otherwise they will be covered up. (a) 3D curved surface of the calculated vegetation depth d_{veg} on different vehicle distance *d* and antenna height H in NLOS area. (b) 2D curve of the calculated vegetation depth d_{veg} on different vehicle distance d and some fixed antenna height H in NLOS area.

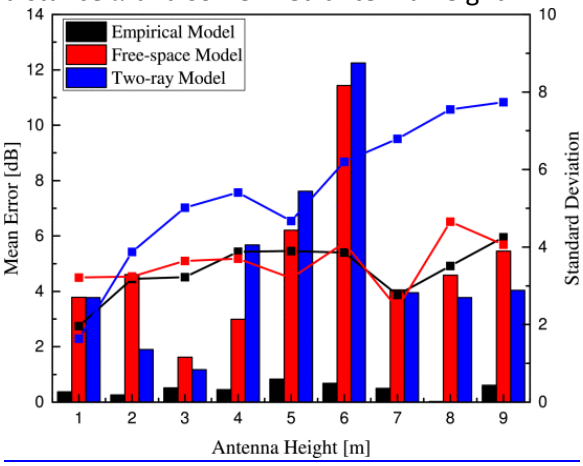

Fig. 8. Error Analysis for three models at nine antenna heights.

- **LOS-B Area.** The measured RSS shows extreme fluctuation in the LOS-B area, and we call this area the "fluctuant area". Although the mean error of the two-ray model is lower than the free-space model, the standard deviation is higher in Fig. 8. This means that the predicted value of the two ray model fluctuates severely around the measured value. Compared with the other two models, the empirical model has advantages of both accuracy and stability.

- **NLOS Area.** The estimation error between the measurements and the two classical models increases to 12 dB in the NLOS area, where the roadside tree canopies severely deteriorate the signal strength. Therefore, we call this area the "occlusion area". The proposed model has a good fitting performance for NLOS area, and the relationship between n_{NLOS} and H can be applied to other similar scenarios.
- **LOS-A Area.** The measured RSS presents a slow-varying trend when the infrastructural height continues to increase. The mean error of both classical models are about 4–5 dB while that of our proposed model is near-zero. We call this area the "stable area". Also, the path loss exponent n_{LOS-A} of the proposed model slightly changes in this area.

Generally, the link quality of V2I communications is best in the LOS-B area (except $H = 1$ m), second in the LOS-A area, and worst in the NLOS area. The analysis results confirmed that the link classification is significant in order to establish a accurate prediction model in V2I scenarios, where the roadside tree canopies constitute the main obstacles that deteriorate the communication quality.

SECTION VI. Small-Scale Fading Analysis for V2I Channel

In this section, we will present the statistical analysis of the small-scale fading for the V2I channel to get a more complete picture of the wireless characteristics. We use two effective methods to statistically model the spatial/temporal short-term fast fading [17], [29], [30]. Firstly, we analyze the fading behavior of the channel, mainly the fading depth. Secondly, we use Ricean distribution to describe the small-scale fading, and model the variations of the distance-dependent Ricean K-factor. We validate the empirical K-factor model with three existing models and finally estimate the values.

A. Fading Depth Analysis

Fading depth measures the variation of the signal energy relative to its local mean due to small scale fading, which is an important channel parameter from the perspective of radio network planning [31]. We present the fading depth of small-scale fading with 10-cm sample interval from measurements based on nine infrastructural heights in Table IV. The fading depth is defined as differences of small-scale fading amplitudes between 50% and 1% [17]. From the table, we observe that in the V2I scenarios, the fading depth is between 4.24 dB and 7.68 dB, this parameter can be used for link budget considerations on system performance and energy requirements [29].

TABLE IV Small-Scale Fading Analysis

Height [m]	Fading Depth [dB]			K-Factor	Fitting
	50 %	1 %	Fading depth	a	b
1	0.08	-5.08	5.16	-0.00304	5.04485
2	0.14	-5 .44	5 .5 8	-0.02737	7.40406
3	0.06	-4.48	4.54	-0.02718	7.22525
4	0.12	-4.1 2	4.24	-0.04285	12.994
5	0.12	-4.42	4.54	-0.05949	14.80356
6	0.02	-5.44	5.46	-0.02433	9.40231
7	0.18	-7.5	7.68	-0.0 1838	8.44158
8	0.1	-4.74	4.84	-0.00967	7.0793
9	0.1	-5.5	5.6	-0.02187	8.1402

B. Ricean K-Factor Analysis

Since abundant LOS links exist in our scenario, we choose the Ricean distribution to characterize the statistical variations of small-scale fading. Although the short-term variations follow the Rayleigh distribution in the NLOS area, the Rayleigh distribution can be considered as a particular case of Ricean distribution. Therefore, we use the more general Ricean distribution to analyze fast fading. The probability distribution function (PDF) of Ricean distribution is as follows:

$$f(r) = \frac{r}{\sigma^2}\exp\left[\frac{-(r^2+s^2)}{2\sigma^2}\right] I_0\left(\frac{rs}{\sigma^2}\right)$$

(29)

where r is the small-scale fading amplitude; $2\sigma^2$ is the average power in the NLOS multipath components; and s^2 is the power in the LOS component. $I_0(\cdot)$ is the modified Bessel function of 0th order, and $K = s^2/2\sigma^2$ denotes the Ricean K-Factor, which measures the fading severity and is very important for link budget predictions. For the case $K = 0$, Ricean fading degenerates into Rayleigh fading, and $K = \infty$ means no multipath fading and only the LOS component exists. In other words, a small K implies severe fading, whereas a large K implies milder fading [27]. We use the moment-based method in [32], [33] to estimate the K-factor, which can be expressed as follows:

$$K = \frac{\sqrt{(E[r^2])^2 - Var[r^2]}}{E[r^2] - \sqrt{(E[r^2])^2 - Var[r^2]}}$$

(30)

where $Var[r^2]$ denotes the variance of r-square. The K-Factor values are extracted from the measurements of the sliding/non-overlapped windows (we set the window size as $40\lambda \approx 5$ m in our experiments according to [29]).

The variability of Ricean K-Factor at different antenna heights is demonstrated with boxplot in Fig. 9. We observe that the mean K-Factor approaches zero even in a clear LOS area, where the signal is affected by the strong reflected ray from the ground. The result is consistent with that of Fig. 8, in which the two-ray model fits better with measurements than the free-space model in the LOS-B and LOS-A areas. The result shows that the reflected components generate non-negligible effects on the received signal power.

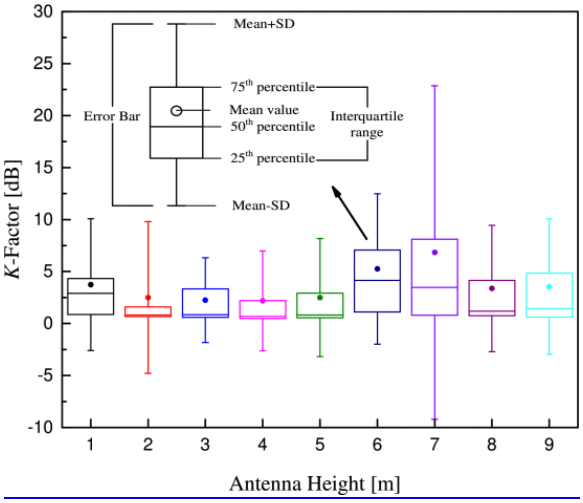

Fig. 9. Boxplot of the Ricean K-Factor at different antenna heights.

Furthermore, in order to study the distance-dependent K-Factor at different antenna heights, we use the linear function $K = a \cdot d + b$ to match the estimated mean values from the first three data sets based on the least-square method in Fig. 10(a). The fitting parameters are listed in Table IV. From the table, it is not hard to find that the slope, a, and the intercept, b, change slightly with H, and we regard their means $\overline{a} = -0.026$ and $\overline{b} = 8.948$ as the constant empirical values. Therefore, the distance-dependent Ricean K-Factor in the V2I scenario can be modeled as the following function:

$$K = 8.948 - 0.026d \tag{31}$$

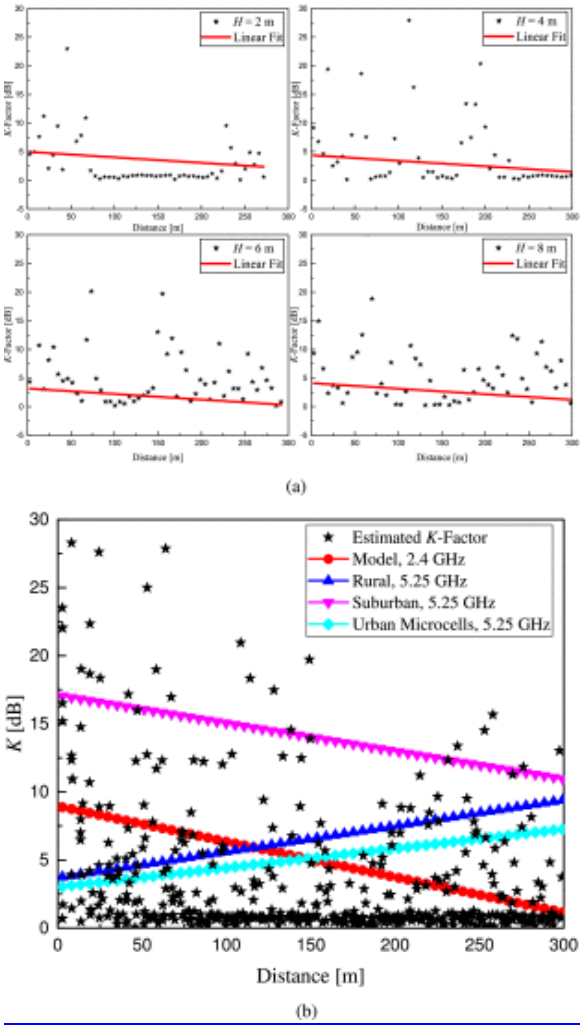

Fig. 10. The linear function is used to fit with the mean K-Factors based on the first three data sets in the upper subgraph, and the model (31) is validated with the fourth data set and three existed models in the lower subgraph. (a) Estimated K-Factor with vehicular distance at different antenna heights. (b) Model validation with estimated K-Factor values and three existed models.

To validate the reasonability of this empirical model, we use the fourth test data and other existing models for comparisons. The three existing models working at 5.25 GHz [34] are presented as follows:

$$K(dB) = \begin{cases} 3.7 + 0.019d & \text{Rural} \\ 17.1 - 0.02d & \text{Suburban} \\ 3 + 0.0142d & \text{Urban Microcells} \end{cases}$$

(32)

From Fig. 10(a), we observe that the K-Factor estimated by the first three data sets approximately decreases with distance at all antenna heights. We find that only our proposed model and existed suburban model maintain this variation tendency in Fig. 10(b), the proposed model is fitted with the estimated Ricean K-factor values at different antenna heights of the fourth data set. The mean error of estimation error verifies that our model is the lowest (1.12 dB) compared with the other three models (2.46 dB, 10.08 dB, and 1.89 dB). Therefore, the model (31) can be used to accurately predict the distance-dependent Ricean K-Factor in the V2I scenario.

SECTION VII. Conclusion

An empirical path loss model for vehicle-to-infrastructure channels is proposed, in which we establish a mathematical connection between the path loss exponent and the antenna height; thereafter, we analyze the shadowing effect for three different link types. Based on the research results, the link-level classification is crucial to accurate predictions of signal attenuation. We also present a statistical analysis of the small-scale fading effect, which is essential for successful deployment of safety applications based on V2I communications. This work applies to the V2I scenario where the roadside row of trees constitutes the main obstruction, prevalently in many urban, suburban and rural streets. In the future, we will explore more realistic environments (i.e., obstructions of vehicles, buildings and pedestrians) which affect V2I communications. It needs to take further measurements to consider all possible cases, more related research should be investigated to fill the V2I channel model library for future VANETs systems.

References

1. K. A. Hafeez, L. Zhao, B. Ma and J. W. Mark, "Performance analysis and enhancement of the DSRC for VANET's safety applications", *IEEE Trans. Veh. Technol.*, vol. 62, no. 7, pp. 3069-3083, Sep. 2013.

2. J. Gao, M. Li, L. Zhao and X. Shen, "Contention intensity based distributed coordination for V2V safety message broadcast", *IEEE Trans. Veh. Technol.*, vol. 67, no. 12, pp. 12 288-12 301, Dec. 2018.

3. W. Xiong, X. Hu and T. Jiang, "Measurement and characterization of link quality for IEEE 802.15.4-compliant wireless sensor networks in vehicular communications", *IEEE Trans. Ind. Informat.*, vol. 12, no. 5, pp. 1702-1713, Oct. 2016.

4. D. Tacconi, D. Miorandi, I. Carreras, F. Chiti and R. Fantacci, "Using wireless sensor networks to support intelligent transportation systems", *Ad Hoc Netw.*, vol. 8, no. 5, pp. 462-473, 2010.

5. J. A. Nazabal, F. Falcone, C. Fernandez-Valdivielso and I. R. Matias, "Development of a low mobility IEEE 802.15.4 compliant VANET system for urban environments", *Sensors*, vol. 13, no. 6, pp. 7065-7078, 2013.

6. I. Bisio, C. Garibotto, F. Lavagetto, A. Sciarrone and S. Zappatore, "Blind detection: Advanced techniques for WiFi-based drone surveillance", *IEEE Trans. Veh. Technol.*, vol. 68, no. 1, pp. 938-946, Jan. 2019.

7. A. F. Molisch, F. Tufvesson, J. Karedal and C. F. Mecklenbrauker, "A survey on vehicle-to-vehicle propagation channels", *IEEE Wireless Commun.*, vol. 16, no. 6, pp. 12-22, Dec. 2009.

8. M. Boban, J. Barros and O. K. Tonguz, "Geometry-based vehicle-to-vehicle channel modeling for large-scale simulation", *IEEE Trans. Veh. Technol.*, vol. 63, no. 9, pp. 4146-4164, Nov. 2014.

9. K. A. Hafeez, L. Zhao, Z. Liao and B. N. Ma, "Impact of mobility on VANETs' safety applications", *Proc. IEEE Global Telecommun. Conf.*, pp. 1-5, Dec. 2010.

10. I. Bisio, A. Delfino, A. Grattarola, F. Lavagetto and A. Sciarrone, "Ultrasounds-based context sensing method and applications over the internet of things", *IEEE Internet Things J.*, vol. 5, no. 5, pp. 3876-3890, Oct. 2018.

11. M. Boban and W. Viriyasitavat, Channel Models for Vehicular Communications, Cham:Springer, pp. 335-363, 2015.

12. W. Viriyasitavat, M. Boban, H. Tsai and A. Vasilakos, "Vehicular communications: Survey and challenges of channel and propagation models", *IEEE Veh. Technol. Mag.*, vol. 10, no. 2, pp. 55-66, Jun. 2015.

13. P. Belanovic, D. Valerio, A. Paier, T. Zemen, F. Ricciato and C. F. Mecklenbrauker, "On wireless links for vehicle-to-infrastructure communications", *IEEE Trans. Veh. Technol.*, vol. 59, no. 1, pp. 269-282, Jan. 2010.

14.J. Maurer, W. SÃ ürgel and W. Wiesbeck, "Ray-tracing for vehicle-to-vehicle communications", *Proc. Ursi*, 2005.

15. G. Acosta-Marum and M. A. Ingram, "Six time- and frequency-selective empirical channel models for vehicular wireless LANs", *IEEE Veh. Technol. Mag.*, vol. 2, no. 4, pp. 4-11, Dec. 2007.

16. A. Chelli, R. Hamdi and M. Alouini, "A vehicle-to-infrastructure channel model for blind corner scattering environments", *Proc. 78th IEEE Veh. Technol. Conf. (VTC Fall)*, pp. 1-6, Sep. 2013.

17. R. He, Z. Zhong, B. Ai and J. Ding, "An empirical path loss model and fading analysis for high-speed railway viaduct scenarios", *IEEE Antennas Wireless Propag. Lett.*, vol. 10, pp. 808-812, 2011.

18. G. Javier, S. Miguel and B. Ramon, "IEEE 802.11p vehicle to infrastructure communications in urban environments", *IEEE Commun. Mag.*, vol. 50, no. 5, pp. 176-183, May 2012.

19. Y. S. Meng, Y. H. Lee and B. C. Ng, "Empirical near ground path loss modeling in a forest at VHF and UHF bands", *IEEE Trans. Antennas Propag.*, vol. 57, no. 5, pp. 1461-1468, May 2009.

20. B. Aygun, M. Boban, J. P. Vilela and A. M. Wyglinski, "Geometry-based propagation modeling and simulation of vehicle-to-infrastructure links", *Proc. IEEE 83rd Veh. Technol. Conf. (VTC Spring)*, pp. 1-5, May 2016.

21. W. Li, X. Hu and T. Jiang, "Path loss models for IEEE 802.15.4 vehicle-to-infrastructure communications in rural areas", *IEEE Internet Things J.*, vol. 5, no. 5, pp. 3865-3875, Oct. 2018.

22. X. Zhao, T. Rautiainen, K. Kalliola and P. Vainikainen, "Path-loss models for urban microcells at 5.3 GHz", *IEEE Antennas Wireless Propag. Lett.*, vol. 5, pp. 152-154, 2006.

23. N. Kato et al., "Location awareness system for drones flying beyond visual line of sight exploiting the 400 MHz frequency band", *IEEE Wireless Commun.*, vol. 26, no. 6, pp. 149-155, Dec. 2019.

24. F. Tang, Z. M. Fadlullah, N. Kato, F. Ono and R. Miura, "AC-POCA: Anticoordination game based partially overlapping channels assignment in combined UAV and D2D-based networks", *IEEE Trans. Veh. Technol.*, vol. 67, no. 2, pp. 1672-1683, Feb. 2018.

25. N. C. Rogers et al., "A generic model of 1-60 GHz radio propagation through vegetation", 2002.

26. C. F. Mecklenbrauker et al., "Vehicular channel characterization and its implications for wireless system design and performance", *Proc. IEEE*, vol. 99, no. 7, pp. 1189-1212, Jul. 2011.

27. A. Goldsmith, Wireless Communications, Cambridge, U.K.:Cambridge Univ. Press, 2005.

28. M. S. Neiman, "The principle of reciprocity in antenna theory", *Proc. IRE*, vol. 31, no. 12, pp. 666-671, Dec. 1943.

29. R. He, Z. Zhong, B. Ai, J. Ding, Y. Yang and A. F. Molisch, "Short-term fading behavior in high-speed railway cutting scenario: Measurements analysis and statistical models", *IEEE Trans. Antennas Propag.*, vol. 61, no. 4, pp. 2209-2222, Apr. 2013.

30. D. Takaishi, Y. Kawamoto, H. Nishiyama, N. Kato, F. Ono and R. Miura, "Virtual cell based resource allocation for efficient frequency utilization in unmanned aircraft systems", *IEEE Trans. Veh. Technol.*, vol. 67, no. 4, pp. 3495-3504, Apr. 2018.

31.F. D. Cardoso and L. M. Correia, "Fading depth evaluation in mobile communications-from GSM to future mobile broadband systems", *Proc. 13th IEEE Int. Symp. Personal Indoor Mobile Radio Commun.*, pp. 125-129, Sep. 2002.

32.A. Abdi, C. Tepedelenlioglu, M. Kaveh and G. Giannakis, "On the estimation of the K parameter for the Rice fading distribution", *IEEE Commun. Lett.*, vol. 5, no. 3, pp. 92-94, Mar. 2001.

33.L. J. Greenstein, S. S. Ghassemzadeh, V. Erceg and D. G. Michelson, " Ricean \$K\$ -factors in narrow-band fixed wireless channels: Theory experiments and statistical models ", *IEEE Trans. Veh. Technol.*, vol. 58, no. 8, pp. 4000-4012, Oct. 2009.

34.D. S. Baum et al., "Final report on link level and system level channel models", *Inf. Soc. Technol.*, 2005.